Nano Research

ISSN 1998-0124 CN 11-5974/O4
https://doi.org/10.26599/NR.2026.94908647

Research Article

Interface modification for silver telluride quantum dots shortwave-infrared photodetectors beyond 1.5 μm

Zhixuan Wang[1,2], Zhiyong Tang[1,2], Ziyan Zhang[1,2], Yejun Zhang[2], Jiang Jiang[1,2], Hongchao Yang[2](✉), Qiangbin Wang[1,2,3,4](✉)

[1] School of Nano-Tech and Nano-Bionics, University of Science and Technology of China, Hefei 230026, China

[2] CAS Key Laboratory of Nano-Bio Interface, Division of Nanobiomedicine and i-Lab, Suzhou Institute of Nano-Tech and Nano-Bionics, Chinese Academy of Sciences, Suzhou 215123, China

[3] School of Physical Science and Technology, ShanghaiTech University, Shanghai 201210, China

[4] College of Materials Sciences and Opto-Electronic Technology, University of Chinese Academy of Sciences, Beijing 100049, China

Nano Res., **Just Accepted Manuscript** • https://doi.org/10.26599/NR.2026.94908647

https://www.sciopen.com/journal/1998-0124 on Mar. 16, 2026

Just Accepted

TABLE OF CONTENTS (TOC)

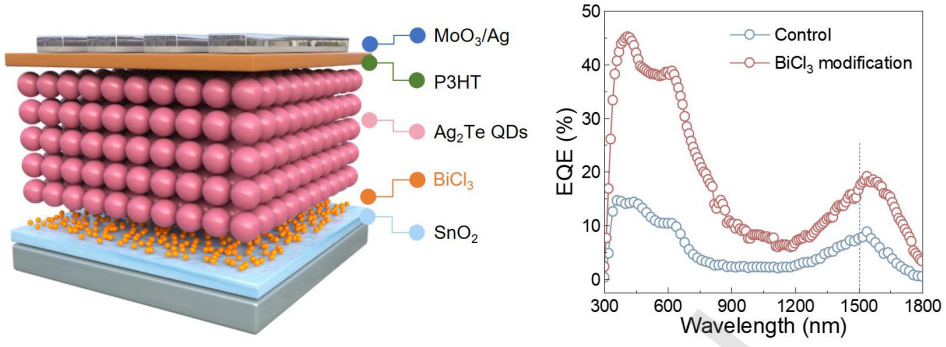

An inorganic bismuth chloride ($BiCl_3$) interface modification of Ag_2Te QD photodiodes achieve a record external quantum efficiency (EQE) of approximately 20% at 1540 nm under zero bias, along with a specific detectivity (D^*) of 2.3×10^{11} Jones at room temperature.

Nano Research

Open Access

Research Article

Interface modification for silver telluride quantum dots shortwave-infrared photodetectors beyond 1.5 μm

Zhixuan Wang[1, 2], Zhiyong Tang[1, 2], Ziyan Zhang[1, 2], Yejun Zhang[2], Jiang Jiang[1, 2], Hongchao Yang[2] and Qiangbin Wang[1, 2, 3, 4]

[1] *School of Nano-Tech and Nano-Bionics, University of Science and Technology of China, Hefei 230026, China*
[2] *CAS Key Laboratory of Nano-Bio Interface, Division of Nanobiomedicine and i-Lab, Suzhou Institute of Nano-Tech and Nano-Bionics, Chinese Academy of Sciences, Suzhou 215123, China*
[3] *School of Physical Science and Technology, ShanghaiTech University, Shanghai 201210, China*
[4] *College of Materials Sciences and Opto-Electronic Technology, University of Chinese Academy of Sciences, Beijing 100049, China*

Received: 10 February 2026; **Revised:** 12 March 2026; **Accepted:** 16 March 2026

Address correspondence to Hongchao Yang, hcyang2014@sinano.ac.cn; Qiangbin Wang, qbwang2008@sinano.ac.cn

Cite this article: *Nano Research*, 2026, 19, 94908647 https://doi.org/10.26599/NR.2026.94908647

ABSTRACT: Solution-processed shortwave-infrared (SWIR) photodetectors utilizing colloidal quantum dots (QDs) represent a transformative advancement in next-generation infrared optoelectronics. Although environmentally benign silver telluride (Ag_2Te) QDs have shown promise for SWIR detection, the performance of such devices, especially beyond 1.5 μm, remains constrained by inadequate energy-level alignment at heterojunctions and insufficient passivation of interfacial defects. This study introduces an inorganic bismuth chloride ($BiCl_3$) interlayer between the SnO_2 electron transport layer and the Ag_2Te QD active layer. This modification simultaneously facilitates effective defect passivation and optimized band alignment, leading to a significant improvement in photocarrier collection efficiency. The resulting $BiCl_3$-modified Ag_2Te QD photodiodes achieve a record external quantum efficiency (EQE) of approximately 20% at 1540 nm under zero bias, along with a specific detectivity (D^*) of 2.3×10^{11} Jones at room temperature. This work provides valuable insights into interface engineering for developing high-performance eco-friendly SWIR QD optoelectronic devices.

KEYWORDS: Short-wave infrared, silver telluride, quantum dots, photodiodes, interface modification

1 Introduction

Shortwave infrared (SWIR, 1.0–2.5 μm) photodetectors, known for their high resolution and strong immunity to optical interference, have attracted significant interest for applications in optical communications[1], night vision[2,3], biomedical imaging[4,5], and chemical analysis[6–8]. Commercial SWIR photodetectors are currently dominated by photosensitive semiconductors such as germanium (Ge), indium gallium arsenide (InGaAs), and mercury cadmium telluride (HgCdTe), typically fabricated via epitaxial growth techniques. Over recent decades, colloidal quantum dot (QD) based SWIR photodetectors have emerged as promising alternatives, offering high intrinsic absorption coefficients, tunable spectral response, cost-effective production, and solution processability[9–12].

Among various materials, silver chalcogenide QDs have attracted considerable attention due to their environmental friendliness, tunable bandgap, and high quantum efficiency[13]. In particular, silver telluride (Ag_2Te) QDs, with a bulk bandgap ($E_{g,bulk}$ = 0.67 eV) and high carrier transport properties, are highly suitable for constructing efficient SWIR photodetectors[14]. Substantial research has focused on optimizing Ag_2Te QD synthesis through doping, core-shell structures for defect passivation[15–17], surface ligand modification for improved charge transport[18,19], and bandgap engineering for targeted light absorption[16]. Despite these efforts, interfacial energy barriers continue to impede carrier transport between Ag_2Te QDs and charge transport layers, reducing photoelectric conversion efficiency and overall device performance. Moreover, rational design of photodiode architectures, particularly concerning interfacial charge dynamics between p-type Ag_2Te QDs and electron transport layers (ETLs), has received limited attention. These interfacial processes critically influence photogenerated carrier separation, extraction, accumulation, and recombination[20,21]. Therefore, achieving optimal energy-level alignment and interfacial defect passivation remains essential for realizing high-performance SWIR Ag_2Te QD photodiodes[22–26].

In this study, we present a novel interfacial modification strategy involving the introduction of $BiCl_3$ at the ETL/Ag_2Te QD interface in a vertical photodiode structure. This approach effectively enhances energy level alignment and passivates interfacial defects. Precise tuning of the energy level structure optimizes the contact potential, resulting in a

two-fold increase in device photocurrent. By implementing this straightforward yet effective interface modification, we achieve an EQE of approximately 20% at 1540 nm and a specific detectivity (D^*) of 2.3×10^{11} Jones under zero bias at room temperature.

2. Experimental

2.1. Chemicals

Silver acetate anhydrous (AgAc, 99%) were purchased from Alfa Aesar. 1-Dodecanethiol (DT; ≥98%) and 3-mercaptopropionic acid (MPA; 99%) from Thermo fisher. Dodecane (≥99%, GC), ethyl acetate (EA, AR grade), bismuth chloride ($BiCl_3$), Acetonitrile (99.9%) and tellurium oxide (TeO_2) were purchased from Aladdin. Methanol (99.5%), anhydrous ethanol (99.7%), and chloroform were purchased from Sinopharm Chemical Reagent Company. All these reagents were of analytical grade and used without further purification.

2.2. Synthesis of Ag_2Te QDs

The tellurium precursor was prepared by dissolving 1.25 mmol TeO_2 into 5 mL dodecanethiol (DT) under heating at 100 °C within a nitrogen environment. In a separate 100 mL three-necked flask, 8 mmol silver acetate (AgAc) was combined with 5 mL dodecane and 10 mL DT. This mixture underwent continuous stirring while being heated to 110 °C under a continuous flow of high-purity nitrogen gas, followed by gradual temperature elevation to 160 °C. During this thermal process, the solution transitioned to a transparent yellow hue. A pre-prepared 0.25 M TeO_2-DT precursor solution was then rapidly introduced into the reaction vessel, triggering an instantaneous color transformation to dark black - a visual confirmation of Ag_2Te quantum dot nucleation. Following 15 minutes of reaction maintenance, the system underwent natural cooling after heat termination. Subsequent purification involved sequential washing with chloroform and methanol through centrifugal separation. Systematic adjustment of precursor proportions enabled controlled modulation of QD dimensions and emission characteristics.

2.3. Material characterization

The morphologies of QDs were examined through a Tecnai G2 F20 S-Twin transmission electron microscopy (TEM) at an acceleration of 200 kV. Powder X-ray diffraction (PXRD) patterns were recorded on a Bruker D8 Advance powder X-ray diffractometer, using Cu-Kα radiation (λ = 1.54056 Å). The absorption spectra were recorded with UV-3600 Plus ultraviolet–visible–near infrared ray (UV–vis–NIR) spectrophotometer (SHIMADZU, JAPAN). XPS data were collected under ultrahigh vacuum (10^{-8}–10^{-9} Torr) by an ESCALAB 250 XI system with a monochromatic X-ray source (Al Kα source, UPS data were obtained on an electron spectrometer using monochromatic HeI radiation at 21.22 eV). High-resolution XPS data were collected from the regions around Ag 3d, Te 3d, Sn 4f, O 1s, Bi 4f and Cl 2p.

2.4. Device fabrication

The glass substrates with a patterned ITO anodes were cleaned sequentially in ultrasonic baths of ethanol, acetone, and isopropanol for 15 min each; and then, the cleaned ITO was subjected to a UV-ozone treatment for 30 min. Subsequently, SnO_2 NPs were spin-coated on the ITO glass at 3000 rpm for 45 s, and finally, annealing at 150 °C for 30 min in ambient air. A 0.2 wt% solution of $BiCl_3$ dissolved in acetonitrile was spin-coated over SnO_2 layer at 2500 rpm for 30 s; then, removal of extra $BiCl_3$ with neat acetonitrile was performed by spin-coating. Four layers of Ag_2Te QDs were further deposited on top of $SnO_2/BiCl_3$ films. For each Ag_2Te QD layer, 40 mg mL^{-1} QD solution was spin coated at 3000 rpm for 30 s and ligand-exchanged with MPA/EA (0.5 vol%) for 30 s, followed by rinsing twice with EA. P3HT layers were spin-coated at 3000 rpm for 45 s using an 8 mg/mL chlorobenzene solution. Under vacuum (<1×10^{-6} torr), the top electrode layers, consisting of 10 nm of MoO_3 and 100 nm of Ag, were successively deposited onto the ITO/SnO_2/$BiCl_3$/QD/P3HT structure by a thermal evaporator at a rate of 0.1 and 1 Å s^{-1}, respectively.

2.5. Device characterization

The J-V characteristics of Ag_2Te QD photodetector was measured on a semiconductor analyzer (Keithley 4200A-SCS). The noise spectral density was measured using a low frequency noise test system (LFN-2000) in RMS average mode. The system comprises a low-noise current amplifier (DHPCA-300, Femto) and a DAQ (NI 6341), with an extremely low noise background of 10^{-16} A/$Hz^{0.5}$. Broadband EQE measurements were performed on the QE-R measurement system (Enlitech), with the Xenon intensity calibrated using standard Si detector and InGaAs detector. The time response of the devices was measured using an oscilloscope (Keysight DSOX1204A) and a transimpedance amplifier (Stanford SR570). A 532 nm laser modulating 1 kHz by a waveform generator (Keysight 33500B) was used as a light source. The TPC decay was measured under 0 V with a 532 nm laser and the pulse width was set to 8 μs and frequency to 20 kHz. Mott-Schottky analysis was conducted based on the measurement of the capacitance-voltage curve. The equipment used was a multichannel potentiometer (VMP300, Biologic), with the test frequency set at 50 kHz, a voltage range of −0.5 to 0.8 V, a step size of 40 mV, and an amplitude of 20 mV. All the device characterizations were performed in air under ambient conditions.

3. Result and Discussions

Colloidal SWIR Ag_2Te QDs were synthesized via a hot-injection method (details provided in Electronic Supplementary Material, ESM). As shown in Fig. S1 in ESM, distinct exciton absorption peaks with tunability were obtained by adjusting the Ag/Te ratio. Transmission electron microscopy (TEM) and powder X-ray diffraction (XRD) confirmed the uniform morphology and monoclinic phase structure of the Ag_2Te QDs[27]. X-ray photoelectron spectroscopy (XPS) in Fig. S2 in ESM confirmed the presence of Ag^+ and Te^{2-} species, with no metallic Ag(0) signals, unequivocally verifying Ag_2Te formation[18,28].

Then, the as-prepared Ag_2Te QDs (absorption peak at ~1400 nm) were incorporated into SWIR photodiodes (Figure S3), and SnO_2 was selected as the electron transport layer (ETL) due to its superior carrier dynamics compared to ZnO (Fig. S4 in ESM). This enhancement stems from the

higher intrinsic electron mobility of SnO_2 (240 $cm^2 \cdot V^{-1} \cdot s^{-1}$ versus 200 $cm^2 \cdot V^{-1} \cdot s^{-1}$ for ZnO), which promotes more efficient electron extraction and transfer[29,30]. Ultraviolet photoelectron spectroscopy (UPS) revealed significant energy band misalignment between SnO_2 and Ag_2Te QDs (Fig. 1a and Fig. S5 in ESM). As illustrated in Fig. 1b(i), the energy barrier at the SnO_2/QD interface is determined by the conduction band offset (CBO) at equilibrium, influenced by the respective Fermi levels. Due to a smaller difference in electron affinity (ΔE_1 = 0.87 eV) relative to the Fermi level difference (ΔE_2 = 1.16 eV), pronounced huge band bending occurs at equilibrium. This leads to carrier accumulation near the SnO_2/QD interface[31,32] and induces severe interface recombination[14], thereby diminishing photo-response efficiency.

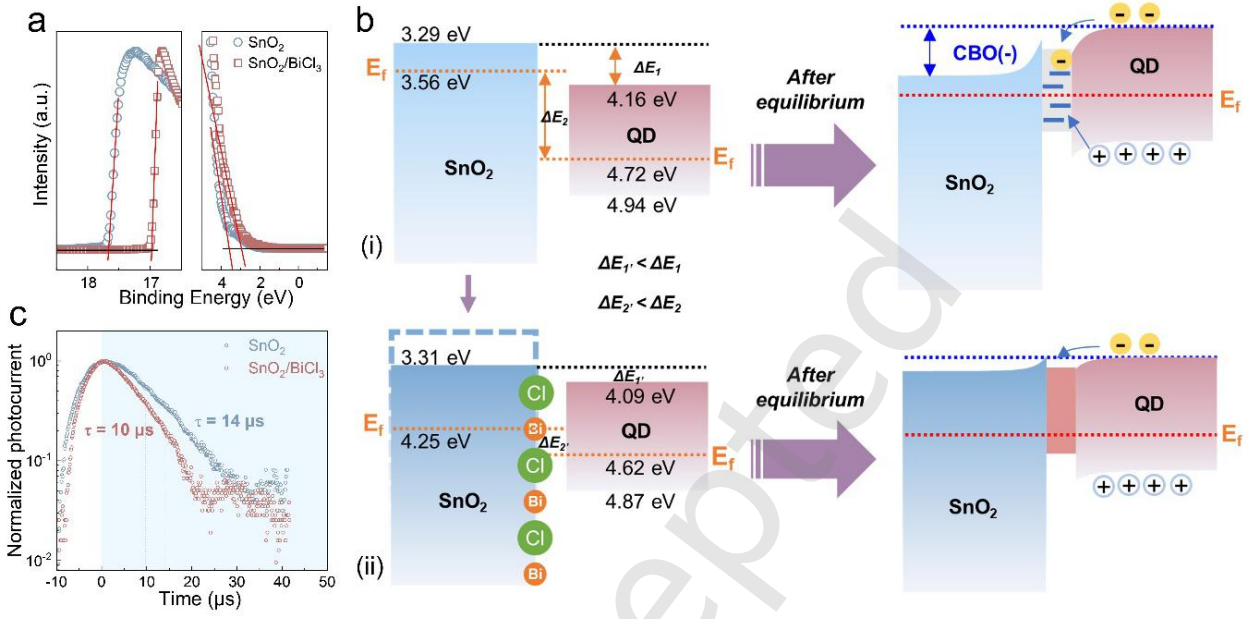

Figure 1. (a) UPS spectra of SnO_2 and $BiCl_3$-modified SnO_2. (b) Schematic illustration of the band bending and built-in electric field formation at the interface with (i) and without (ii) $BiCl_3$ treatment. (c) Transient photocurrent decay curves of Ag_2Te QD photodiodes with and without $BiCl_3$ treatment.

To address this issue, we introduced an interfacial modification by spin-coating $BiCl_3$ at an optimized concentration onto the SnO_2 ETL (Figs. S6–S8 in ESM). Atomic force microscopy (AFM) and scanning electron microscopy (SEM) confirmed that the $BiCl_3$-modified SnO_2 films remained continuous, pinhole-free, and smooth (Figs. S9–S11 in ESM), ensuring efficient electron transport. After $BiCl_3$ treatment, the Fermi level of SnO_2 shifted downward from –3.56 eV to –4.25 eV, accompanied by a downward adjustment of its conduction band (Fig. 1a). This evolution arises from the cooperative effects of Bi^{3+} and Cl^- at the interface. Mechanistically, Bi^{3+} is electrostatically adsorbed on Sn vacancy, increasing the positive charge density at the SnO_2 surface and pushing the Fermi level toward the valence band. In parallel, Cl^- mainly serves to balance the charge, and it will adsorb onto the surface of SnO_2 or be embedded in the lattice, which inhibits the formation of oxygen vacancies (oxygen vacancies are the main source of free electrons in n-type SnO_2). This reduction in oxygen vacancies contributes to the downward shift of the Fermi level. As a result, the conduction band position of SnO_2 decreases, and its electron affinity increases (Fig. 1b(ii)). At equilibrium, the conduction band alignment between the QDs and modified SnO_2 became more favorable, resulting in reduced band bending and minimizing the accumulation of interface charges, which in turn, effectively suppresses interfacial recombination. This minimized CBO facilitates efficient charge extraction while maintaining a sufficient energy barrier to suppress back electron transfer and interfacial recombination[22,31]. Additionally, the close alignment of Fermi levels between the QDs and modified SnO_2 ensures a sufficient valence band offset from the SnO_2 conduction band even under reverse bias, further inhibiting interfacial recombination. These findings highlight the importance of precise energy-level tuning for enhancing carrier extraction in narrow-bandgap semiconductor systems[33,34].

Transient photocurrent decay measurements were conducted to validate the improved carrier extraction efficiency. As shown in Fig. 1c, the decay time decreased markedly from 14 μs to 10 μs after $BiCl_3$ treatment, indicating enhanced charge extraction and suppressed interfacial recombination[29]. Electrochemical impedance spectroscopy (EIS) further supported these results, revealing inhibited recombination dynamics at the SnO_2/Ag_2Te QD heterojunction. Fig. S12 in ESM and its inset present Nyquist plots and equivalent circuits for devices with and without $BiCl_3$ modification. The high-frequency intercept corresponds to series resistance (R_s), while the low-frequency arc relates to recombination resistance (R_{rec}). The reduced R_s and increased R_{rec} in $BiCl_3$-modified devices (Table S1 in ESM) confirm improved charge transport efficiency[35].

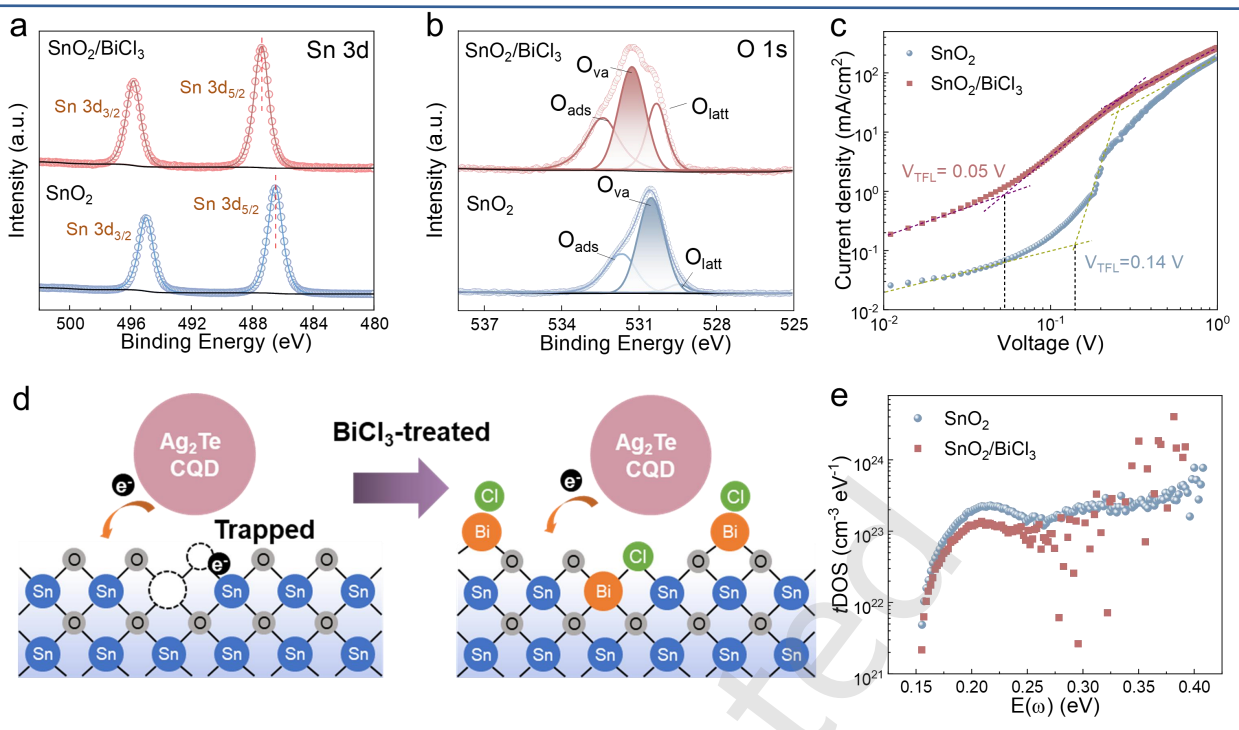

Figure 2. High-resolution XPS spectra of (a) Sn 3d and (b) O 1s for the SnO_2 film and $BiCl_3$-modified SnO_2 film. (c) *J*–*V* curves of the electron-only devices based on the control device and $BiCl_3$-modified device using the SCLC technique. (d) Schematic illustration of $BiCl_3$-modified SnO_2. (e) *t*DOS distribution of Ag_2Te QD photodiodes with and without $BiCl_3$ treatment.

Interfacial defect passivation also plays a crucial role in carrier recombination dynamics. SnO_2 films often contain intrinsic point defects (dominant defects of oxygen vacancies, interstitial Sn, and undercoordinated Sn sites), which may introduce trap states that promote nonradiative recombination and hinder charge extraction[36,37]. To investigate the effect of $BiCl_3$ treatment, XPS analysis was performed. The survey spectrum (Fig. S13 in ESM) confirmed the presence of Bi and Cl elements only on treated SnO_2, indicating successful modification. High-resolution Sn 3d spectra (Fig. 2a) showed a positive binding energy shift, suggesting enhanced electron withdrawal from Sn^{4+} centers due to Sn–Cl coordination, which passivates surface Sn dangling bonds[35]. This electron withdrawal is further supported by the role of Bi^{3+}, which, due to its higher electronegativity, draws electron density from the surface through occupying Sn vacancy sites. Deconvolution of O 1s spectra (Fig. 2b) revealed three components: adsorbed oxygen, oxygen vacancies, and lattice oxygen. Cl^- ions primarily serve to balance the charge by adsorbing onto SnO_2 surface or embedding into the lattice, which inhibits the formation of oxygen vacancies. Consequently, the surface concentration of oxygen vacancies decreased significantly from 75% to 45% after modification (Table S2 in ESM), confirming effective passivation. This reduction in oxygen vacancies, coupled with the passivation of Sn dangling bonds, significantly reduces electron-trapping defects at the interface and further suppress interfacial recombination. Furthermore, positive binding energy shifts in Ag 3d and Te 3d regions (Figs. S14a-b in ESM) suggest charge redistribution via coordination with Bi^{3+} and/or Cl^-, indicating synergistic interface stabilization through Lewis acid–base interactions. We consider this treatment represents a surface modification of the Ag_2Te QD film.

Space-charge-limited current (SCLC) measurements further elucidated the electronic impact of defect passivation. Fig. S15 in ESM shows that the modified SnO_2 film exhibited reduced trap density while maintaining similar electron mobility. Consequently, the $BiCl_3$-treated electron-only devices displayed a smaller trap filled limit voltage (V_{TFL}) (Fig. 2c), accompanied by decreased trap density and increased electron mobility (Table S3 in ESM), indicating suppressed trap-limited transport as illustrated in Fig. 2d. Thermal admittance spectroscopy (TAS) provided additional insight into the trap density of states (*t*DOS)[38]. The energetic profile of *t*DOS, derived from capacitance-frequency measurements[39], depicts significant deep trap densities in the devices without $BiCl_3$ treatment (Fig. 2e), primarily arising from the intrinsic defects in Ag_2Te QDs[40]. And the *t*DOS also shows a lower peak value of 1.28×10^{23} cm^{-3} eV^{-1} for the $BiCl_3$-treated device, particularly at shallow energy levels. This confirms effective interface trap passivation and consistent with improved charge transfer kinetics.

Having demonstrated that $BiCl_3$ treatment improves both energy-level alignment and interfacial defect passivation, we systematically evaluated its impact on photodiode performance. The device structure was ITO/SnO_2/Ag_2Te QDs/P3HT/MoO_3/Ag[41], as depicted in Fig. 3a. The Ag_2Te QD layer underwent solid-state ligand exchange with 3-mercaptopropionic acid (MPA) to serve as the SWIR photoactive layer. Cross-sectional SEM (CS-SEM) imaging indicated a QD layer thickness of approximately 135 nm (Fig. 3b, Fig. S16 in ESM). Under 1532 nm laser illumination, the $BiCl_3$-treated device exhibited a over twofold increase in photocurrent compared to the untreated device (Fig. 3c), consistent with enhanced charge extraction and suppressed recombination. The dark current density of the $BiCl_3$-treated

device is 2×10^{-2} mA/cm^2 at −0.3 V reverse bias, which is only slightly lower than that of the untreated device (Fig. 3d). This indicates that the dark current appears insensitive to the $BiCl_3$ treatment. We think this is because although the $BiCl_3$ modification inhibits the interface recombination, it also increases the work function of ETLs, leading to weakened built-in electric fields, thereby counteracting the effect of carrier recombination. As depicted in Fig. 3e and Fig. S17 in ESM, the EQE analysis revealed a peak value of approximately 20% at 1540 nm under zero bias for the treated device and only 8% for the control. This value demonstrates competitive performance of the modified photodiodes compared to previously reported QD devices (Table S4 in ESM). The enhancement of the device's EQE is primarily attributed to the reduction of interface defect states and the suppression of recombination.

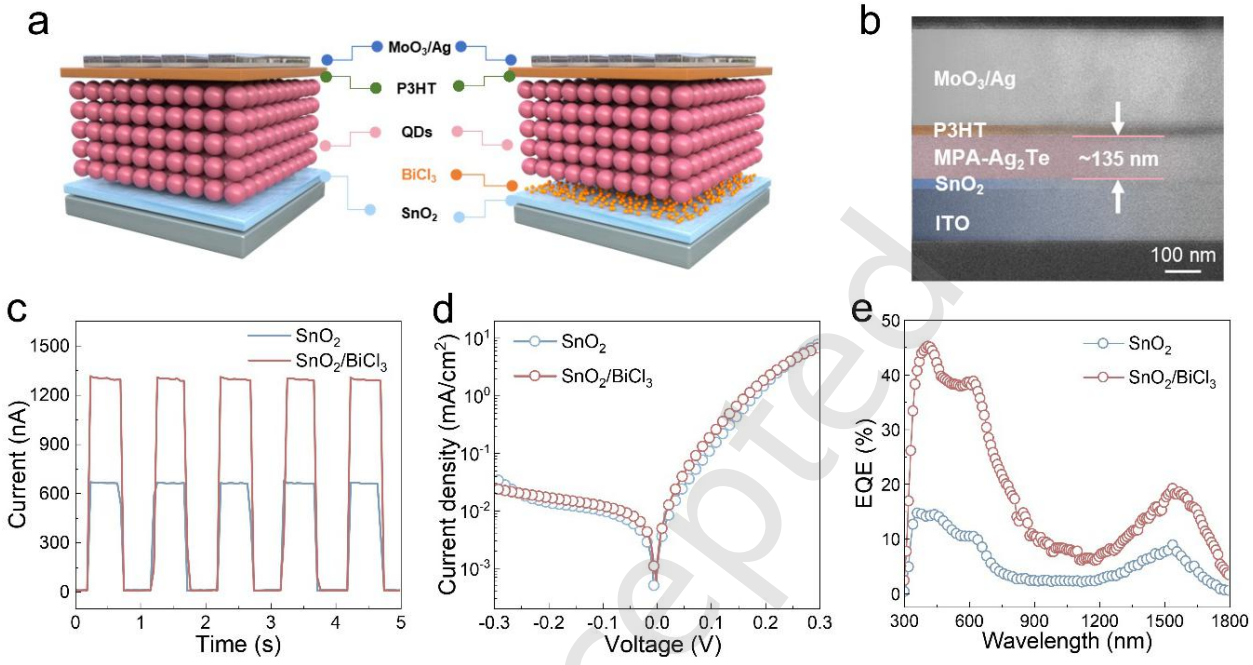

Figure 3. (a) Schematic illustration of the Ag_2Te QD photodiodes device structure. (b) Cross-sectional SEM image of the photodiodes. (c) On-off characteristics under short-circuit conditions with a 1532 nm irradiation of Ag_2Te QD photodiodes with and without $BiCl_3$ treatment. (d) Dark current density-voltage (*J*-*V*) curves of photodiodes with and without $BiCl_3$ treatment. (e) Broadband external quantum efficiency (EQE) spectra of Ag_2Te QD photodiodes with and without $BiCl_3$ treatment.

The specific detectivity (D^*) was calculated using the formula[42]: $D^* = R\times(A\times\Delta f)^{1/2}/i_n$, where R is responsivity, i_n is noise current (at 1 Hz), A is device area (0.06 cm^2), and Δf is electrical bandwidth (1 Hz). The frequency-dependent noise spectral density was measured using a low-frequency noise test system (LFN-2000, Wuxi Xinjian Semiconductor Technology Co., Ltd.) in RMS average mode. The system comprises a low-noise current amplifier (DHPCA-300, Femto) and a DAQ (NI 6341), with an extremely low noise background of 10^{-16} A/Hz$^{0.5}$ at 1 Hz (Fig. S18 in ESM)[43–45]. As shown in Fig. S16 in ESM, the noise current characteristics for the two photodiodes remains nearly unchanged, which agrees with the dark current in Fig. 3d. And the noise current of the optimized device measured at 0 V was 4×10^{-13} A/Hz$^{0.5}$ at 1 Hz, which was used in the calculation of D^*. The optimized device achieved a responsivity of 0.22 A/W at 1540 nm under zero bias (Fig. S19 in ESM), corresponding to a D^* of 2.3×10^{11} Jones (Fig. 4a). The linear dynamic range (LDR) exceeded 92 dB (Fig. 4b), demonstrating excellent performance across a broad illumination range. Transient response measurements further reveal the rise and fall times of 13 μs and 9 μs for the $BiCl_3$ modified devices under modulated light excitation (Fig. 4c). The frequency-dependent response was measured at 0 V bias, showing a -3dB bandwidth at 41.7 kHz (Fig. 4d), which is consistent with the response speed. We believe that further reducing the device area and optimizing the device structure by eliminating the organic charge transport layer will further enhance the device's response speed. Figs. S20 and S21 in ESM indicate the well uniformity and stability of the optimized devices without encapsulation in an ambient air environment.

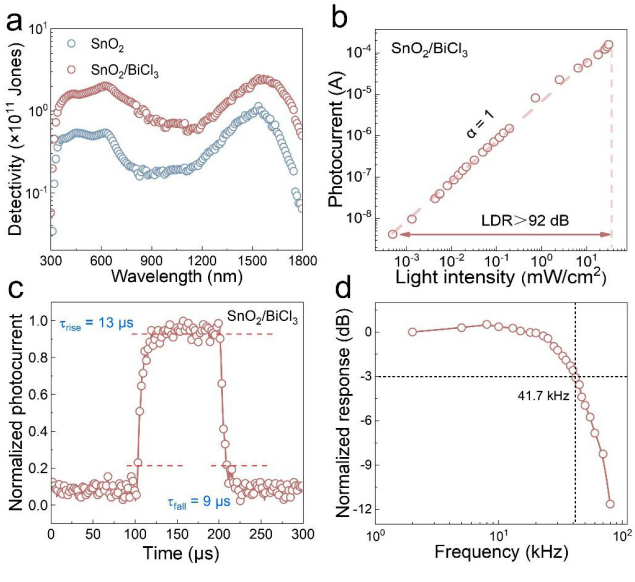

Figure 4. (a) Broadband Specific detectivity spectra of Ag_2Te QD photodiodes with and without $BiCl_3$ treatment. (b) LDR of $BiCl_3$-treated

Ag_2Te QD photodiode under 1532 nm illumination with power densities from ~1.3 μW cm^{-2} to ~32 mW cm^{-2}. Response speed (c) and bandwidth (d) characterization of the Ag_2Te QD photodiodes.

To illustrate practical applicability, we integrated the optimized photodetectors into an optical communication system for ASCII code transmission (Fig. 5a)[46]. Using a 1532 nm laser with computer-controlled modulation, we generated binary data streams encoding "WANGLAB". The Ag_2Te photodiode successfully detected these signals and converted them into electrical outputs, which were decoded back to the original characters (Fig. 5b). Moreover, the SWIR communication system exhibited superior anti-interference capability compared to visible-light systems (Figs. 5c–d), highlighting the potential of these eco-friendly QD photodiodes in real-world applications.

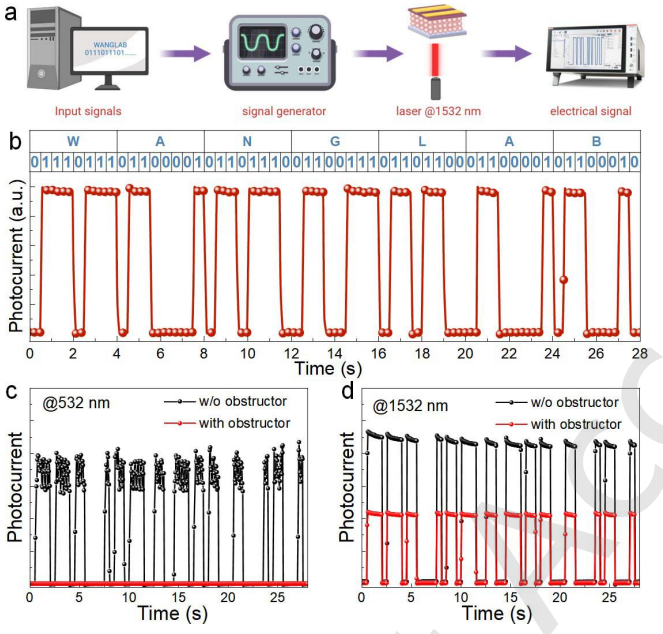

Figure 5. (a) Schematic diagram of SWIR optical communication applications. (b) Transmission of ASCII code (WANGLAB) information using the optimal photodiode device as the signal receiver under 1532 nm light illumination. (c, d) Anti interference capability of the SWIR devices. The photocurrent of the optimal photodiode device with and without silicon obstructor under (c) 1532 nm and (d) 532 nm laser.

4. Conclusion

In summary, we developed a high-performance SWIR photodetector based on Ag_2Te QDs through interface modification with $BiCl_3$. This treatment optimized energy level alignment and passivated interfacial defects, effectively suppressing interface recombination during photo-excited charge carrier transfer to the ETL. The optimized device achieved an EQE of approximately 20% at 1540 nm under zero bias and room temperature, along with a specific detectivity of 2.3×10^{11} Jones. This study represents a significant advancement in Ag_2Te QD-based photodetectors and offers a promising interfacial engineering strategy for future optoelectronic devices.

Electronic Supplementary Material: Supplementary material (Additional discussions of characterization, including absorption spectra, XRD pattern, TEM, SEM, AFM images, EDS spectra, UPS analysis, XPS spectra, J-V curves, and C-V characteristics.) is available in the online version of this article at https://doi.org/10.26599/NR.xxxx.949xxxxx (automatically inserted by the publisher).

Data availability

All data needed to support the conclusions in the paper are presented in the manuscript and/or the Electronic Supplementary Material. Additional data related to this paper may be requested from the corresponding author upon request.

Acknowledgments

This work was financially supported by the National Key Research and Development Program of China (Grant Nos. 2024YFA1803402), the National Natural Science Foundation of China (Grant Nos. 22271308, 22127808), the Basic Research Program of Jiangsu Province (Grant Nos. BK20240124). The authors are grateful for the technical support from the Vacuum Interconnected Nanotech Workstation (Nano-X) of Suzhou Institute of Nano-Tech and Nano-Bionics, Chinese Academy of Sciences (SINANO).

Declaration of competing interest

All the contributing authors report no conflict of interests in this work.

Author contribution statement

Hongchao Yang and Qiangbin Wang conceived the concept and supervised the project. Zhixuan Wang, Zhiyong Tang, and Ziyan Zhang synthesized the materials and conducted the structural and optical measurements. Zhixuan Wang fabricated the devices and collected the performance data of the photodiodes. Zhixuan Wang, Hongchao Yang, Yejun Zhang, Jiang Jiang and Qiangbin Wang conducted the data analysis. Zhixuan Wang and Hongchao Yang drafted the manuscript. All authors participated in the scientific discussion and revised the manuscript.

Informed consent

Not applicable.

Ethics statement

Not applicable.

Use of AI statement

None.

References

[1] H. Sargent, E. Infrared quantum dots. *Adv. Mater.* **2005**, *17*, 515–522.

[2] Liu, J.; Liu, P.; Chen, D.; Shi, T.; Qu, X.; Chen, L.; Wu, T.; Ke, J.; Xiong, K.; Li, M.; Song, H.; Wei, W.; Cao, J.; Zhang, J.; Gao, L.; Tang, J. A near-infrared colloidal quantum dot imager with monolithically integrated readout circuitry. *Nat. Electron.* **2022**, *5*, 443–451.

[3] Wang, Y.; Liu, J.; Ran, X.; Lu, H.; Liu, J.; Yang, J.; Xia, H.; Zhang, X.; Zhang, J.; Gao, L.; Long, G.; Hu, H.; Tang, J.; Lan, X. Inorganic ZnTe Hole Transport Layer for PbS Quantum Dot Infrared Photodetectors and Imagers. *Adv. Funct. Mater.* **2025**, *35*, 2426082.

[4] Cosco, E. D.; Spearman, A. L.; Ramakrishnan, S.; Lingg, J. G. P.; Saccomano, M.; Pengshung, M.; Arús, B. A.; Wong, K. C. Y.; Glasl, S.;

Ntziachristos, V.; Warmer, M.; McLaughlin, R. R.; Bruns, O. T.; Sletten, E. M. Shortwave infrared polymethine fluorophores matched to excitation lasers enable non-invasive, multicolour in vivo imaging in real time. *Nat. Chem.* **2020**, *12*, 1123–1130.

[5] Bruns, O. T.; Bischof, T. S.; Harris, D. K.; Franke, D.; Shi, Y.; Riedemann, L.; Bartelt, A.; Jaworski, F. B.; Carr, J. A.; Rowlands, C. J.; Wilson, M. W. B.; Chen, O.; Wei, H.; Hwang, G. W.; Montana, D. M.; Coropceanu, I.; Achorn, O. B.; Kloepper, J.; Heeren, J.; So, P. T. C.; Fukumura, D.; Jensen, K. F.; Jain, R. K.; Bawendi, M. G. Next-generation in vivo optical imaging with short-wave infrared quantum dots. *Nat. Biomed. Eng.* **2017**, *1*, 1–11.

[6] Chen, M.; Lu, H.; Abdelazim, N. M.; Zhu, Y.; Wang, Z.; Ren, W.; Kershaw, S. V.; Rogach, A. L.; Zhao, N. Mercury telluride quantum dot-based phototransistor enabling high-sensitivity room-temperature photodetection at 2000 nm. *ACS Nano* **2017**, *11*, 5614–5622.

[7] Zhang, Z. Y.; Yang, H. C.; Wang, M. Z.; Zhang, Y. J.; Jiang, J.; Wang, Q. B. NIR-II silver-based quantum dots: Synthesis and applications. *Nano Res*. **2024**, *17*, 10620-10643.

[8] Pejović, V.; Georgitzikis, E.; Lee, J.; Lieberman, I.; Cheyns, D.; Heremans, P.; Malinowski, P. E. Infrared colloidal quantum dot image sensors. *IEEE Trans. Electron Dev.* **2022**, *69*, 2840–2850.

[9] Konstantatos, G.; Howard, I.; Fischer, A.; Hoogland, S.; Clifford, J.; Klem, E.; Levina, L.; Sargent, E. H. Ultrasensitive solution-cast quantum dot photodetectors. *Nature* **2006**, *442*, 180–183.

[10] Tang, X.; Ackerman, M. M.; Chen, M.; Guyot-Sionnest, P. Dual-band infrared imaging using stacked colloidal quantum dot photodiodes. *Nat. Photonics* **2019**, *13*, 277–282.

[11] Konstantatos, G.; Sargent, E. H. Nanostructured materials for photon detection. *Nat. Nanotechnol.* **2010**, *5*, 391–400.

[12] Kim, B.; Lee, S. Y.; Ko, H.; Lee, J.; Song, H.; Cho, S.; Kim, Y. H.; Lee, M.-H.; Lee, J.-Y. Ultrahigh-gain colloidal quantum dot infrared avalanche photodetectors. *Nat. Nanotechnol.* **2024**, *20*, 1–9.

[13] Yang, H.; Ma, Z.; Wang, Q. Shortwave-infrared silver chalcogenide quantum dots for optoelectronic devices. *ACS Nano* **2024**, *18*, 30123–30131.

[14] Wang, Y.; Peng, L.; Schreier, J.; Bi, Y.; Black, A.; Malla, A.; Goossens, S.; Konstantatos, G. Silver telluride colloidal quantum dot infrared photodetectors and image sensors. *Nat. Photonics* **2024**, *18*, 236–242.

[15] Kim, G.; Choi, D.; Eom, S. Y.; Song, H.; Jeong, K. S. Extended short-wavelength infrared photoluminescence and photocurrent of nonstoichiometric silver telluride colloidal nanocrystals. *Nano Lett.* **2021**, *21*, 8073–8079.

[16] Liu, Z. Y.; Zhao, W.; Chen, L. M.; Chen, Y. Y.; Wang, Z. G.; Liu, A. A.; Pang, D. W. Rational design and structural regulation of near-infrared silver chalcogenide quantum dots. *Nano Res.* **2024**, *17*, 10585–10606.

[17] Yuan, D.; Cao, F.; Han, Z.; Liu, M.; Deng, X.; Zhang, L.; Liu, X.; Cao, S.; Liu, X.; Yang, Z.; Deng, Z.; Li, Y.; Voznyy, O.; Fan, Q.; Sun, B.; Huang, W. Zinc halide enables highly monodisperse Ag_2Te colloidal quantum dots for short-wave infrared photodetectors. *Nano Energy* **2025**, *140*, 111026.

[18] Ahn, Y.; Eom, S. Y.; Kim, G.; Lee, J. H.; Kim, B.; Kim, D.; Si, M.; Yang, M.; Jung, Y.; Kim, B. S.; Chung, Y. J.; Jeong, K. S.; Baek, S. Silver telluride colloidal quantum dot solid for fast extended shortwave infrared photodetector. *Adv. Sci.* **2024**, *11*, 2407453.

[19] Kim, G.; Choi, D.; Eom, S. Y.; Jung, E. D.; Lee, J. H.; Rehl, B.; Kim, S. Y.; Hoogland, S.; Sargent, E. H.; Jeong, K. S. Extended short-wavelength infrared ink by surface-tuned silver telluride colloidal quantum dots and their infrared photodetection. *ACS Mater. Lett.* **2024**, *6*, 4988–4996.

[20] Choi, J.; Kim, Y.; Jo, J. W.; Kim, J.; Sun, B.; Walters, G.; García de Arquer, F. P.; Quintero-Bermudez, R.; Li, Y.; Tan, C. S.; Quan, L. N.; Kam, A. P. T.; Hoogland, S.; Lu, Z.; Voznyy, O.; Sargent, E. H. Chloride passivation of ZnO electrodes improves charge extraction in colloidal quantum dot photovoltaics. *Adv. Mater.* **2017**, *29*, 1702350.

[21] Wang, Y.; Wu, H.; Rodà, C.; Peng, L.; Taghipour, N.; Dosil, M.; Konstantatos, G. Shortwave infrared light detection and ranging using silver telluride quantum dots. *Adv. Mater.* **2025**, *37*, 2500977.

[22] Shao, S.; Loi, M. A. The role of the interfaces in perovskite solar cells. *Adv. Mater. Interfaces* **2020**, *7*, 1901469.

[23] Khan, J.; Yang, X.; Qiao, K.; Deng, H.; Zhang, J.; Liu, Z.; Ahmad, W.; Zhang, J.; Li, D.; Liu, H.; Song, H.; Cheng, C.; Tang, J. Low-temperature-processed SnO_2–Cl for efficient PbS quantum-dot solar cells via defect passivation. *J. Mater. Chem. A* **2017**, *5*, 17240–17247.

[24] Xu, K.; Ke, L.; Dou, H.; Xu, R.; Zhou, W.; Wei, Q.; Sun, X.; Wang, H.; Wu, H.; Li, L.; Xue, J.; Chen, B.; Weng, T.-C.; Zheng, L.; Yu, Y.; Ning, Z. Large photomultiplication by charge-self-trapping for high-response quantum dot infrared photodetectors. *ACS Appl. Mater. Interfaces* **2022**, *14*, 14783–14790.

[25] Jung, E. H.; Chen, B.; Bertens, K.; Vafaie, M.; Teale, S.; Proppe, A.; Hou, Y.; Zhu, T.; Zheng, C.; Sargent, E. H. Bifunctional surface engineering on sno_2 reduces energy loss in perovskite solar cells. *ACS Energy Lett.* **2020**, *5*, 2796–2801.

[26] Lu, S.; Liu, P.; Yang, J.; Liu, S.; Yang, Y.; Chen, L.; Liu, J.; Liu, Y.; Wang, B.; Lan, X.; Zhang, J.; Gao, L.; Tang, J. High-performance colloidal quantum dot photodiodes via suppressing interface defects. *ACS Appl. Mater. Interfaces* **2023**, *15*, 12061–12069.

[27] Zhou, Y. F.; Huang, B.; Chen, S. H.; Liu, S. L.; Zhang, M. X.; Cui, R. Ultra-bright near-infrared-IIb emitting Zn-doped Ag_2Te quantum dots for noninvasive monitoring of traumatic brain injury. *Nano Res.* **2023**, *16*, 2719-2727.

[28] Yang, H.; Huang, H.; Ma, X.; Zhang, Y.; Yang, X.; Yu, M.; Sun, Z.; Li, C.; Wu, F.; Wang, Q. Au - doped Ag_2Te quantum dots with bright NIR-IIb fluorescence for in situ monitoring of angiogenesis and arteriogenesis in a hindlimb ischemic model. *Adv. Mater.* **2021**, *33*, 2103953.

[29] Jiang, Q.; Zhang, L.; Wang, H.; Yang, X.; Meng, J.; Liu, H.; Yin, Z.; Wu, J.; Zhang, X.; You, J. Enhanced electron extraction using SnO_2 for high-efficiency planar-structure $HC(NH_2)_2PbI_3$-based perovskite solar cells. *Nat. Energy* **2016**, *2*, 1–7.

[30] Tiwana, P.; Docampo, P.; Johnston, M. B.; Snaith, H. J.; Herz, L. M. Electron mobility and injection dynamics in mesoporous ZnO, SnO_2, and TiO_2 films used in dye-sensitized solar cells. *ACS Nano* **2011**, *5*, 5158–5166.

[31] Raoui, Y.; Ez-Zahraouy, H.; Kazim, S.; Ahmad, S. Energy level engineering of charge selective contact and halide perovskite by modulating band offset: Mechanistic insights. *J. Energy Chem.* **2021**, *54*, 822–829.

[32] Ding, C.; Zhang, Y.; Liu, F.; Kitabatake, Y.; Hayase, S.; Toyoda, T.; Yoshino, K.; Minemoto, T.; Katayama, K.; Shen, Q. Effect of the conduction band offset on interfacial recombination behavior of the planar perovskite solar cells. *Nano Energy* **2018**, *53*, 17–26.

[33] Jung, Y.; Shin, H.; Baek, S.-W.; Tai, T. B.; Scheffel, B.; Ouellette, O.; Biondi, M.; Hoogland, S.; García De Arquer, F. P.; Sargent, E. H. Near-unity broadband quantum efficiency enabled by colloidal quantum dot/mixed-organic heterojunction. *ACS Energy Lett.* **2023**, *8*, 2331–2337.

[34] Kim, S.-H.; Lee, D.; Moon, S.; Choi, J.-H.; Kim, D.; Kim, J.; Baek, S.-W. Sulfurized colloidal quantum dot/tungsten disulfide multi-dimensional heterojunction for an efficient self-powered visible-to-SWIR photodetector. *Adv. Funct. Mater.* **2023**, *33*, 2303778.

[35] Xu, M. P.; Chen, D. S.; Lin, J.; Lu, X. Y.; Deng, Y. Z.; He, S. Y.; Zhu, X. T.; Jin, W. X.; Jin, Y. Z. Quantum-dot light-emitting diodes with Fermi-level pinning at the hole-injection/hole-transporting interfaces. *Nano Res.* **2022**, *15*, 7453-7459.

[36] Park, S. Y.; Zhu, K. Advances in SnO_2 for efficient and stable n–i–p

perovskite solar cells. *Adv. Mater.* **2022**, *34*, 2110438.

[37] Kılıç, Ç.; Zunger, A. Origins of coexistence of conductivity and transparency in SnO_2. *Phys. Rev. Lett.* **2002**, *88*, 095501.

[38] Jiang, Y.; Qin, C.; Cui, M.; He, T.; Liu, K.; Huang, Y.; Luo, M.; Zhang, L.; Xu, H.; Li, S.; Wei, J.; Liu, Z.; Wang, H.; Kim, G.-H.; Yuan, M.; Chen, J. Spectra stable blue perovskite light-emitting diodes. *Nat. Commun.* **2019**, *10*, 1868.

[39] Ma, Z.; Sun, Z.; Yang, H.; Wang, Z.; Ren, F.; Yin, N.; Chen, Q.; Zhang, Y.; Li, C.; Chen, L.; Wang, Q. Interface-mediation-enabled high-performance near-infrared AgAuSe quantum dot light-emitting diodes. *J. Am. Chem. Soc.* **2023**, *145*, 24972–24980.

[40] Yang, H.; Li, R.; Zhang, Y.; Yu, M.; Wang, Z.; Liu, X.; You, W.; Tu, D.; Sun, Z.; Zhang, R.; Chen, X.; Wang, Q. Colloidal alloyed quantum dots with enhanced photoluminescence quantum yield in the NIR-II window. *J. Am. Chem. Soc.* **2021**, *143*, 2601–2607.

[41] Han, L.; Ma, Z.; Wang, Z.; Zhang, Z.; Yang, X.; Tang, Z.; Liu, T.; Jiang, J.; Zhang, Y.; Yang, H. Ternary Ag_3AuS_2 nanocrystals for thin-film solar cells. *Inorg. Chem.* **2024**, *63*, 19382–19389.

[42] Saran, R.; Curry, R. J. Lead sulphide nanocrystal photodetector technologies. *Nat. Photonics* **2016**, *10*, 81–92.

[43] Jiang, H.; Hu, Y.; Jiang, H.; Wei, T.; Wang, K.; Chen, L.; Zhang, Q.; Lei, Y. Unidirectional Bias‐Switchable Dual‐Mode Organic Photodetectors Enables Secure Communication and Gesture Simulation. *Adv. Funct. Mater.* **2025**, *35*, 2419686.

[44] Jiang, Y.; Song, Y.; Zhang, Y.; Yu, L.; Zhang, S.; Li, X.; Song, X.; Xia, C. Ferroelectric‐Switchable Single Photodetector Implementing Complex Optoelectronic Logics. *Adv. Funct. Mater.* **2025**, *35*, 2418248.

[45] Liang, J.; Wang, H.; Yin, Z.; Jia, M.; Wang, M.; Yan, D.; Hou, X.; Zhang, J. High detectivity ternary near-infrared organic photodetectors based on double electron transport layer for health monitoring. *J. Mater. Chem. C* **2025**, *13*, 3917–3926.

[46] Liu, X.; Deng, C.; Wei, H.; Fang, M.; Yan, B.; Zhu, T.; Luo, S.; Peng, G.; Cai, W.; Long, M.; Zhang, X. High‐sensitive uncooled mid-wave infrared photodetector based on $PtSe_2/MoTe_2$ heterojunction with fast speed. *Adv. Funct. Mater.* **2025**, *35*, 2423102.

Electronic Supplementary Material

Interface modification for silver telluride quantum dots shortwave-infrared photodetectors beyond 1.5 μm

Zhixuan Wang[1, 2], Zhiyong Tang[1, 2], Ziyan Zhang[1, 2], Yejun Zhang[2], Jiang Jiang[1, 2], Hongchao Yang[2] and Qiangbin Wang[1, 2, 3, 4]

[1] *School of Nano-Tech and Nano-Bionics, University of Science and Technology of China, Hefei 230026, China*
[2] *CAS Key Laboratory of Nano-Bio Interface, Division of Nanobiomedicine and i-Lab, Suzhou Institute of Nano-Tech and Nano-Bionics, Chinese Academy of Sciences, Suzhou 215123, China*
[3] *School of Physical Science and Technology, ShanghaiTech University, Shanghai 201210, China*
[4] *College of Materials Sciences and Opto-Electronic Technology, University of Chinese Academy of Sciences, Beijing 100049, China*

Address correspondence to Hongchao Yang, hcyang2014@sinano.ac.cn; Qiangbin Wang, qbwang2008@sinano.ac.cn

Supporting information to https://doi.org/10.26599/NR.2026.94908647

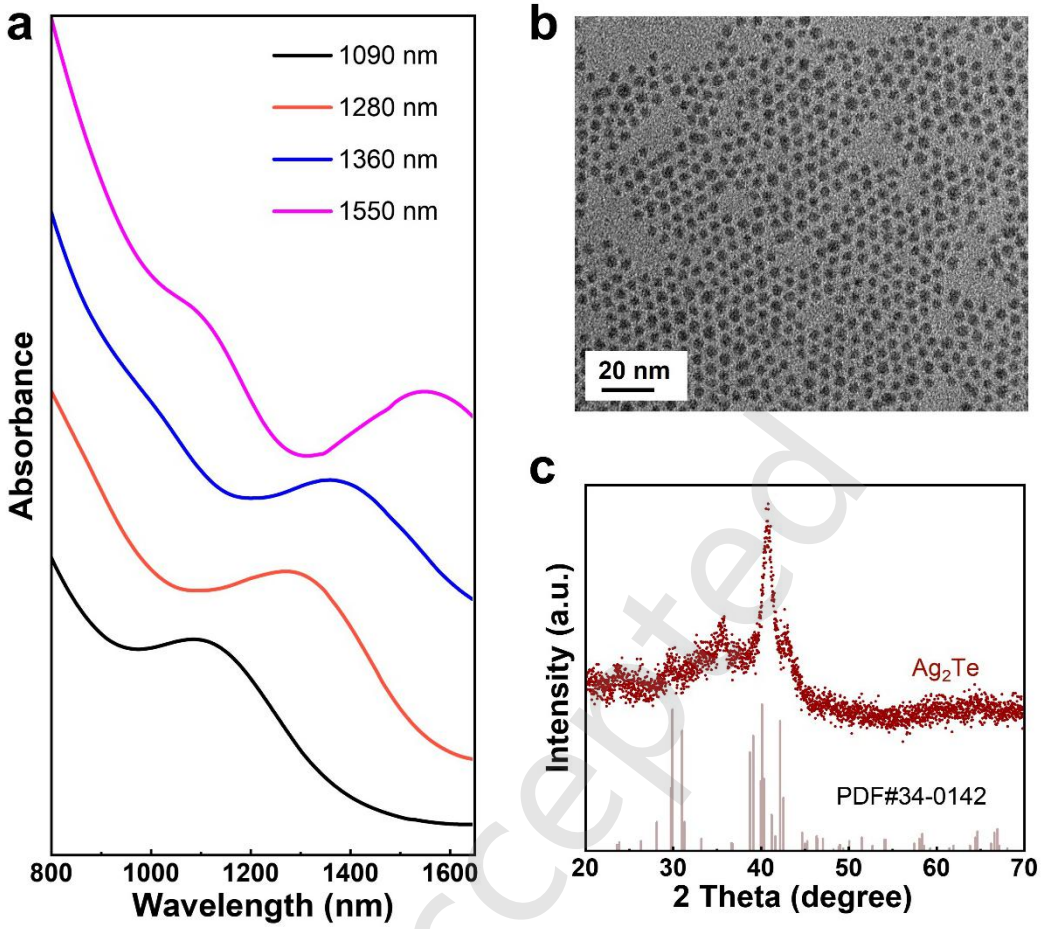

Figure S1. (a) Absorption spectra of Ag_2Te QDs with different sizes. (b) TEM image and (c) XRD pattern of Ag_2Te QDs with exciton absorption peak at 1550 nm.

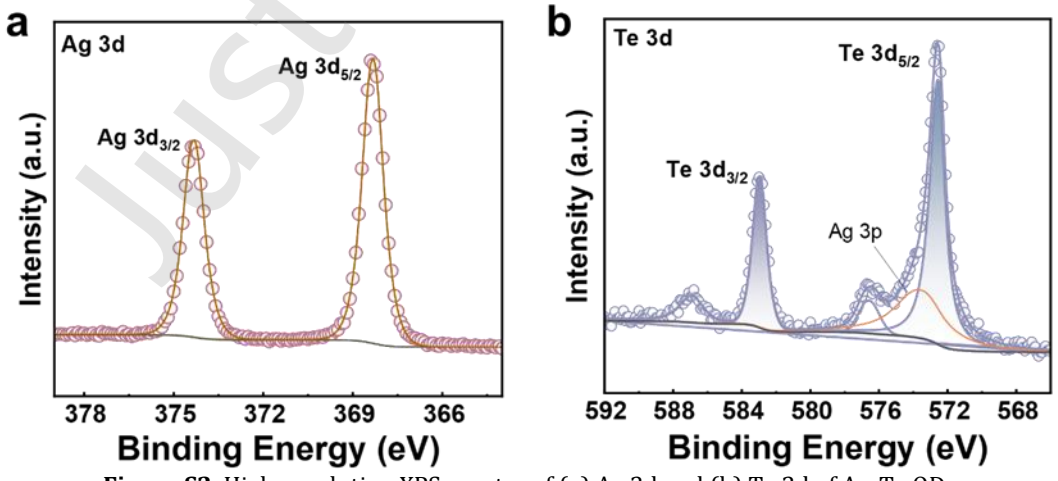

Figure S2. High-resolution XPS spectra of (a) Ag 3d and (b) Te 3d of Ag_2Te QDs.

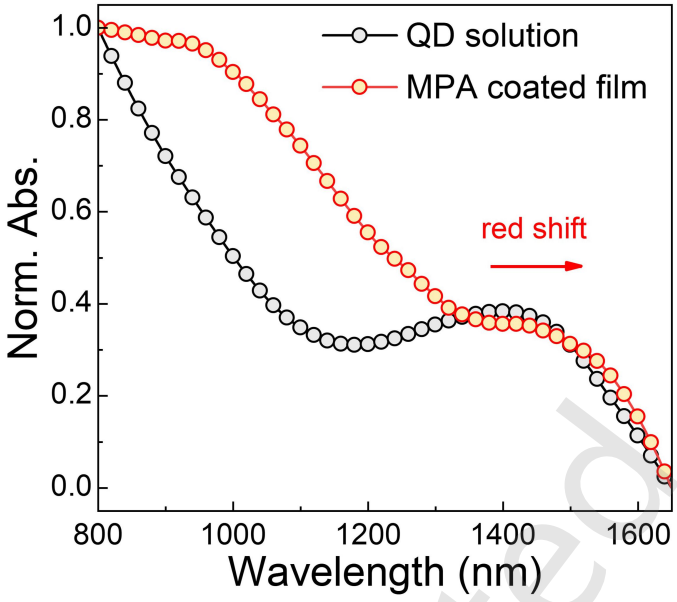

Figure S3. Absorption spectra of Ag_2Te QDs solutions and a single-layer CQD solid film.

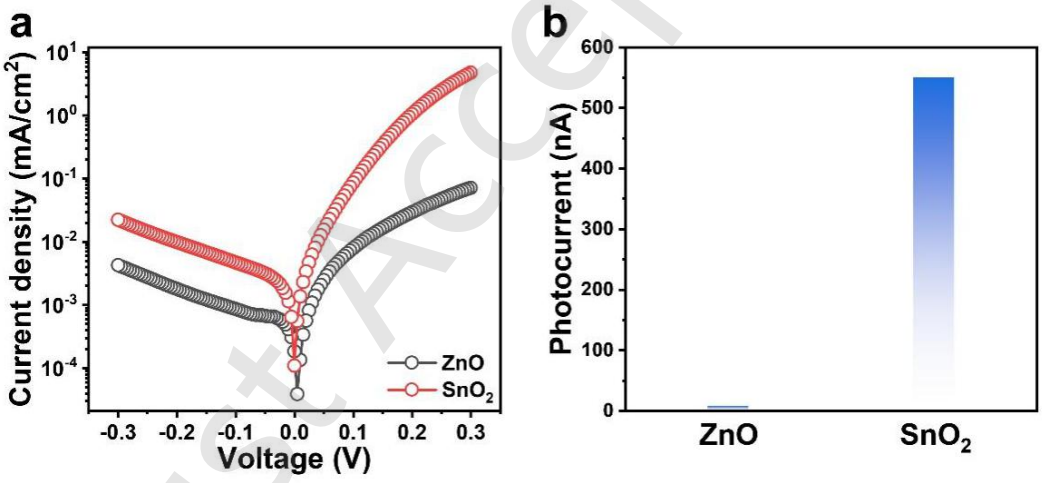

Figure S4. (a) Dark current density-voltage (J-V) curve of control photodiodes with different ETL. (b) Photocurrent of control photodiodes with different ETL under 1532 nm illumination with power densities of 0.09 mW cm^{-2}.

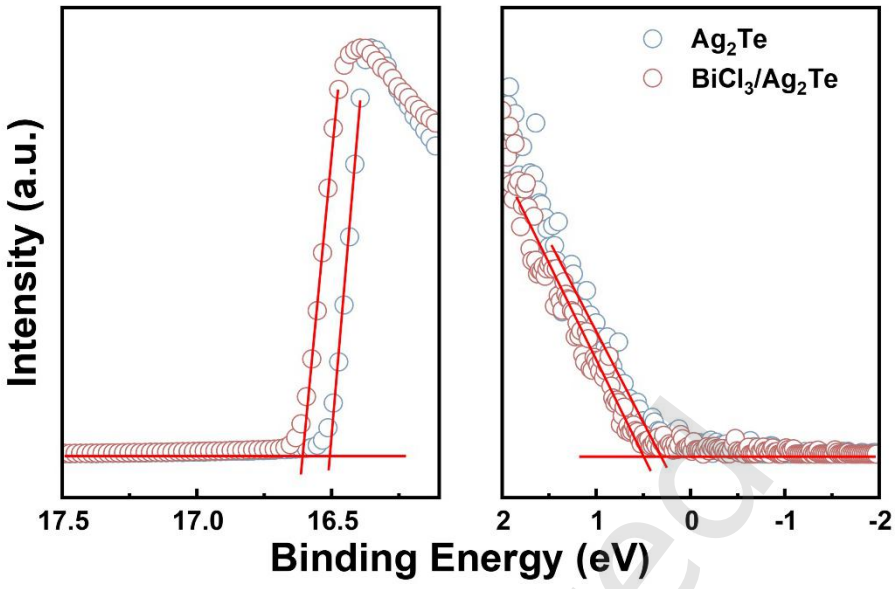

Figure S5. UPS spectra of Ag_2Te. After $BiCl_3$-treatment under MPA-Ag_2Te, the Fermi level shifts upward from 4.73 eV to 4.62 eV.

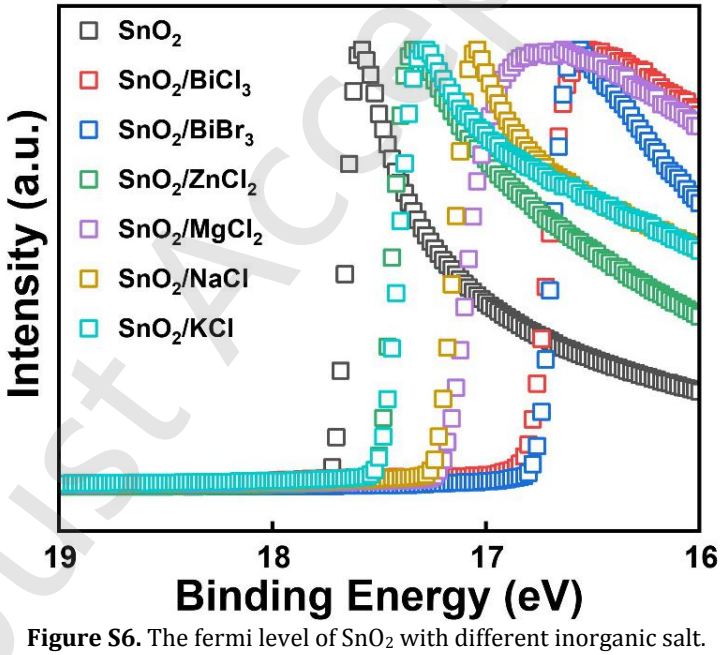

Figure S6. The fermi level of SnO_2 with different inorganic salt.

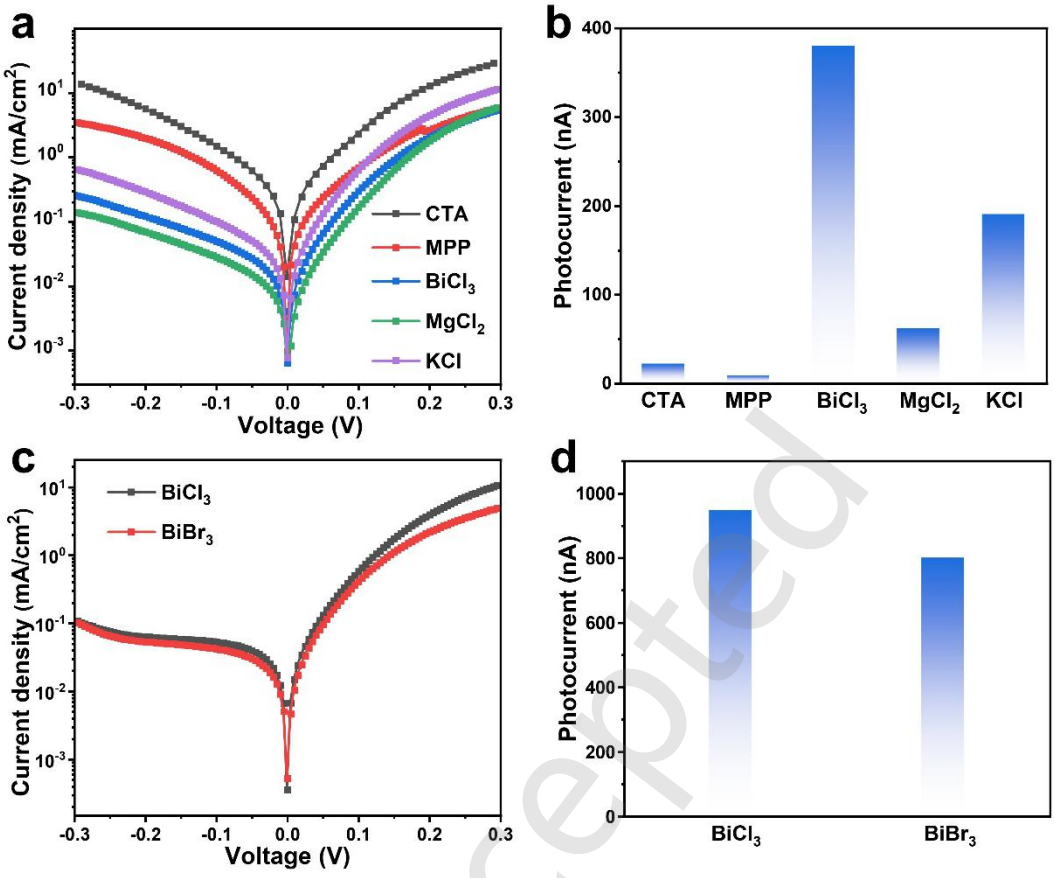

Figure S7. Different organic molecules and inorganic salts interface modification results. Dark J-V curves (a) and Photocurrent (b) of photodiodes with different interface modification. Dark J-V curves (c) and Photocurrent (d) of photodiodes with $BiCl_3$ and $BiBr_3$.

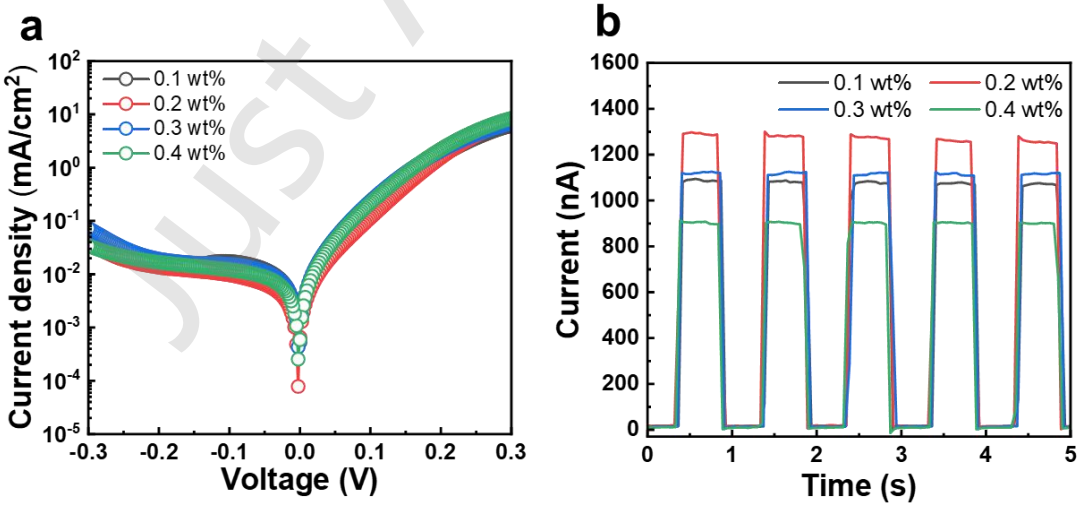

Figure S8. (a) Dark current density-voltage (J-V) curves of photodiodes with $BiCl_3$ treatments with different concentrations. (b) On-off characteristics under short-circuit conditions with a 1532 nm irradiation of photodiodes with $BiCl_3$ treatments with different concentrations.

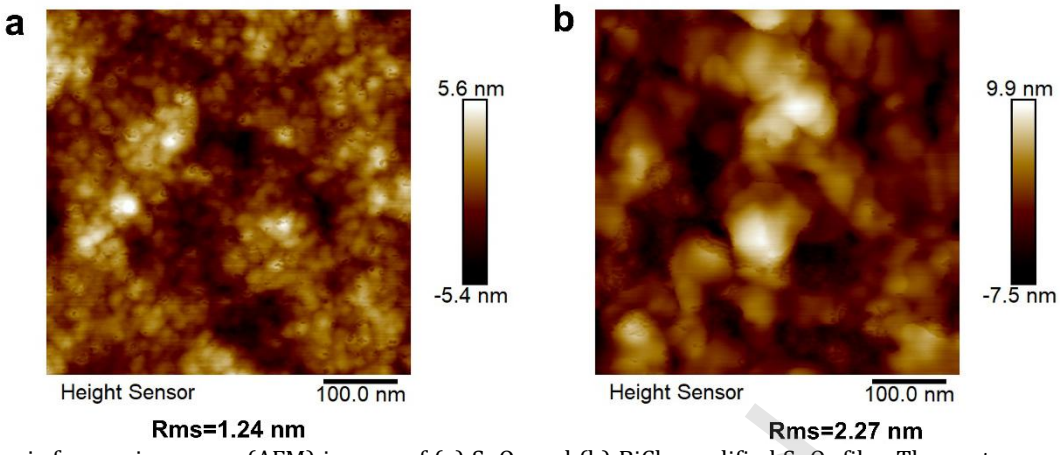

Figure S9. Atomic force microscopy (AFM) images of (a) SnO_2 and (b) $BiCl_3$-modified SnO_2 film. The root mean squared (Rms) roughness of these films is marked under images, respectively. The scan of all images is 500 nm×500 nm.

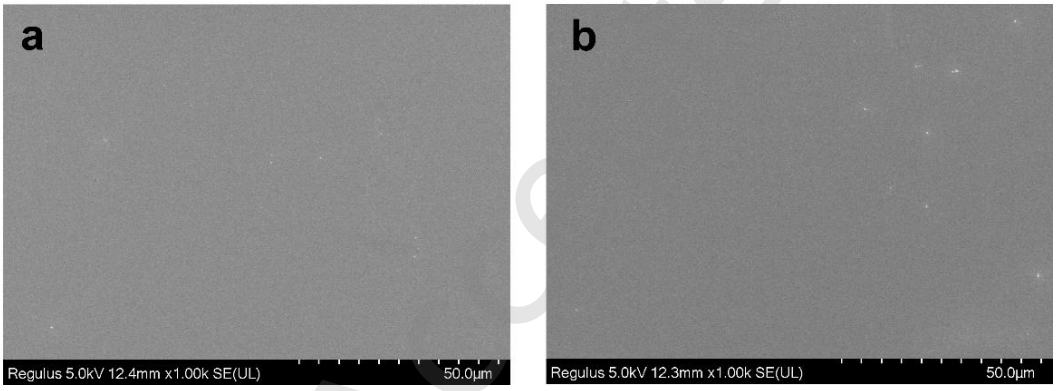

Figure S10. Scanning electron microscopy (SEM) images of (a) SnO_2 and (b) $BiCl_3$-modified SnO_2 film.

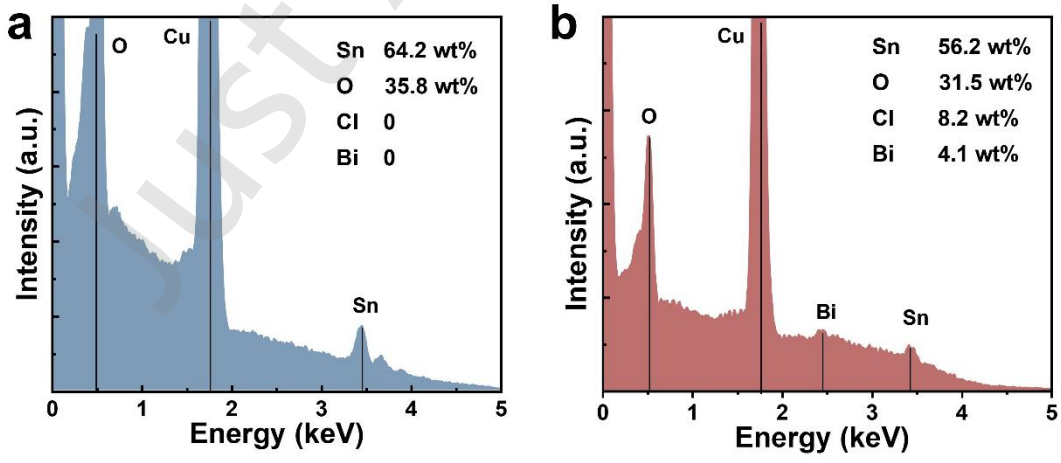

Figure S11. Energy dispersive X-ray spectroscopy (EDS) results of (a) SnO_2 and (b) $BiCl_3$-modified SnO_2 film.

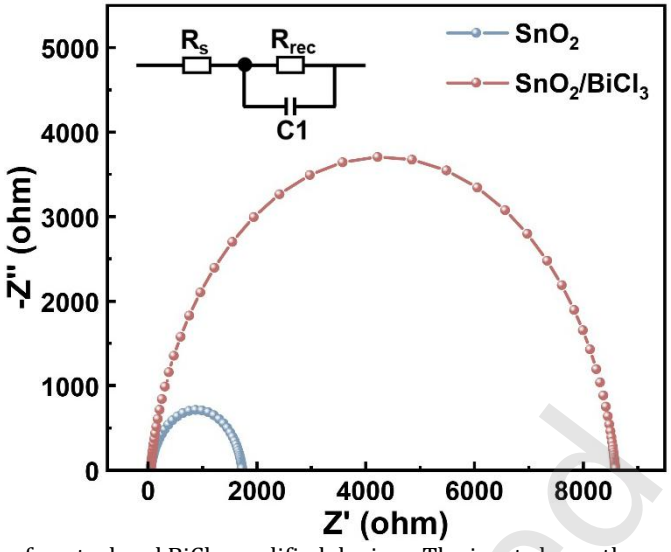

Figure S12. Nyquist plots of control and $BiCl_3$-modified devices. The inset shows the equivalent circuit diagram.

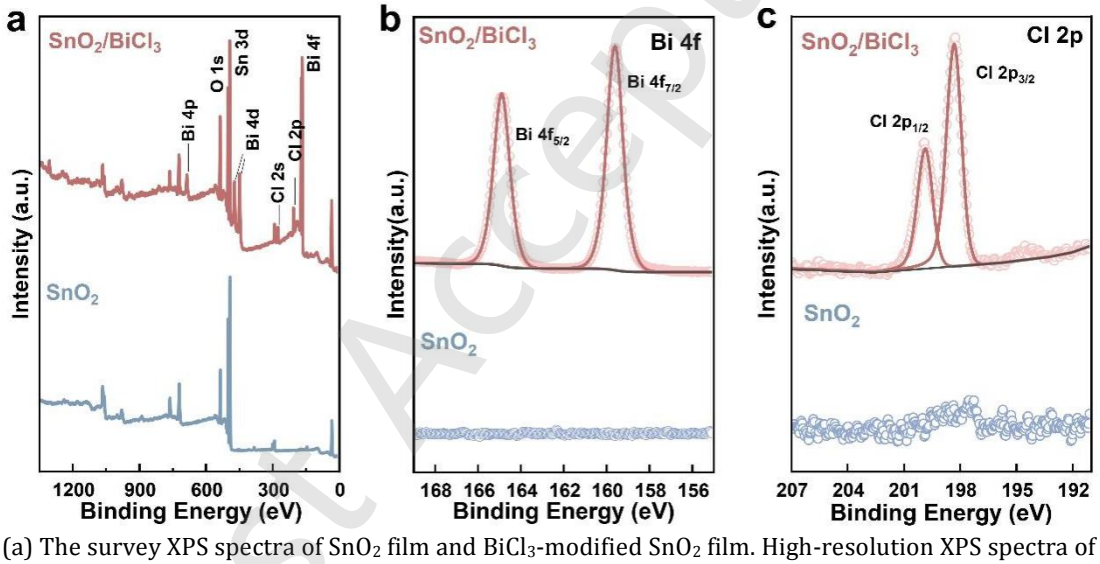

Figure S13. (a) The survey XPS spectra of SnO_2 film and $BiCl_3$-modified SnO_2 film. High-resolution XPS spectra of b) Bi 4f and c) Cl 2p for the SnO_2 film and $BiCl_3$-modified SnO_2 film. Distinct Bi 4f and Cl 2p signals were detected on the SnO_2 thin film through XPS analysis, confirming the successful deposition of $BiCl_3$ onto the SnO_2 surface.

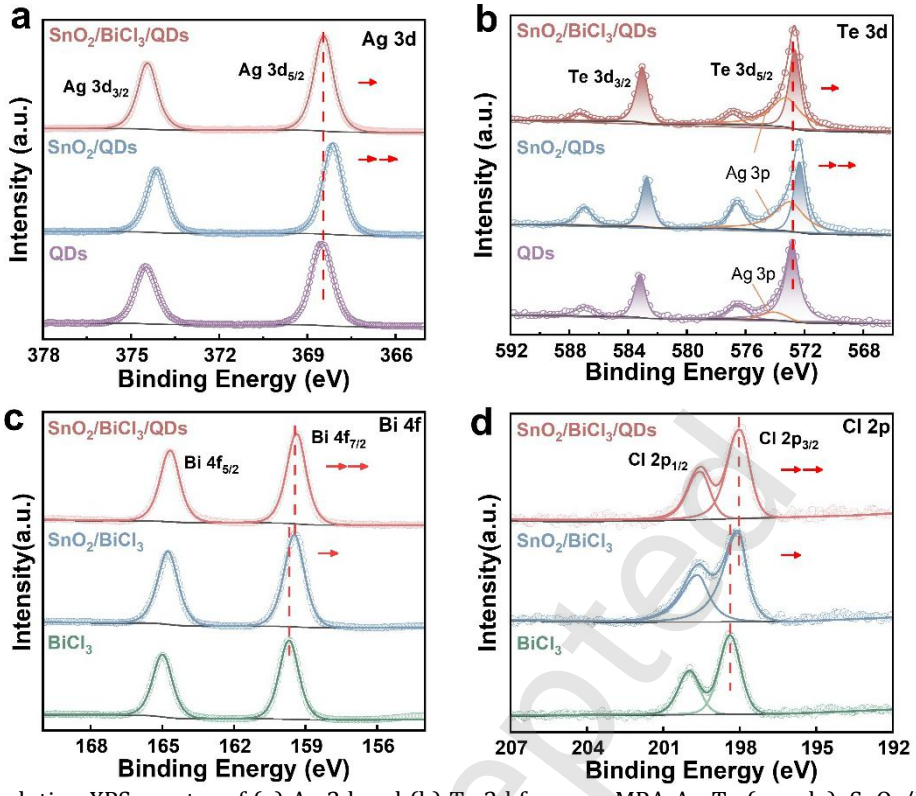

Figure S14. High-resolution XPS spectra of (a) Ag 3d and (b) Te 3d for pure MPA-Ag_2Te (purple), SnO_2/MPA-Ag_2Te film(blue) and SnO_2/$BiCl_3$/MPA-Ag_2Te film (red). High-resolution XPS spectra of (c) Bi 4f and (d) Cl 2p for pure $BiCl_3$ film(green), SnO_2/$BiCl_3$ film(blue) and SnO_2/$BiCl_3$/MPA-Ag_2Te film(red).

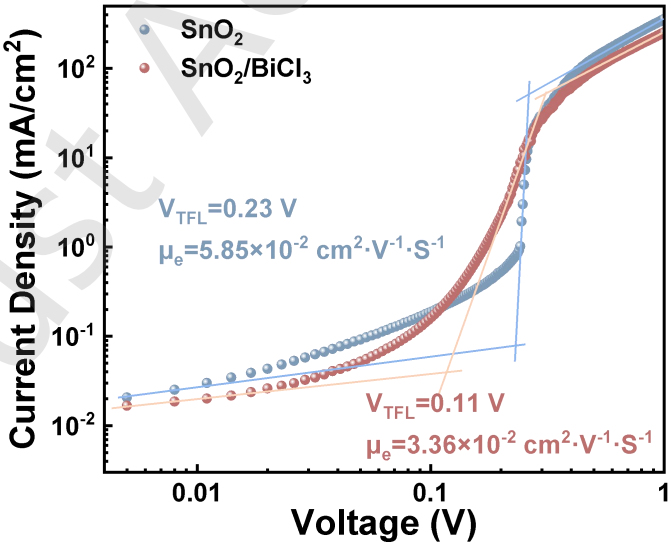

Figure S15. *J*–*V* curves of the electron-only devices based on SnO_2 film and $BiCl_3$-modified SnO_2 film.

The N_{traps} values are extracted from the current density-voltage profiles by the SCLC model, determining by the equation[1]:

$$N_{traps} = \frac{2\varepsilon\varepsilon_0 V_{TFL}}{eL^2}$$

where V_{TFL} is trap-filled limit voltage, e is the elementary charge, L is the film thickness, ε is the relative dielectric constant, and ε_0 is the vacuum permittivity.

The carrier mobility (μ) is extracted from the child region, and determined by the equation:

$$\mu = \frac{8JL^3}{9\varepsilon\varepsilon_0 V^2}$$

where J is the device's current density, and L is the film thickness.

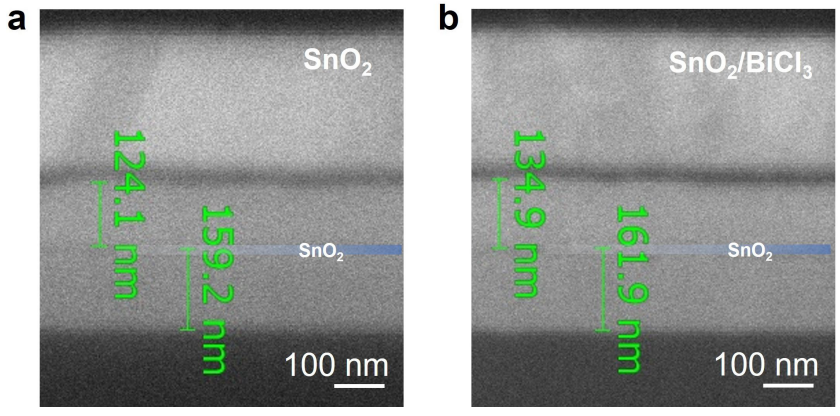

Figure S16. CS-SEM image of the photodiodes before and after $BiCl_3$ treatment.

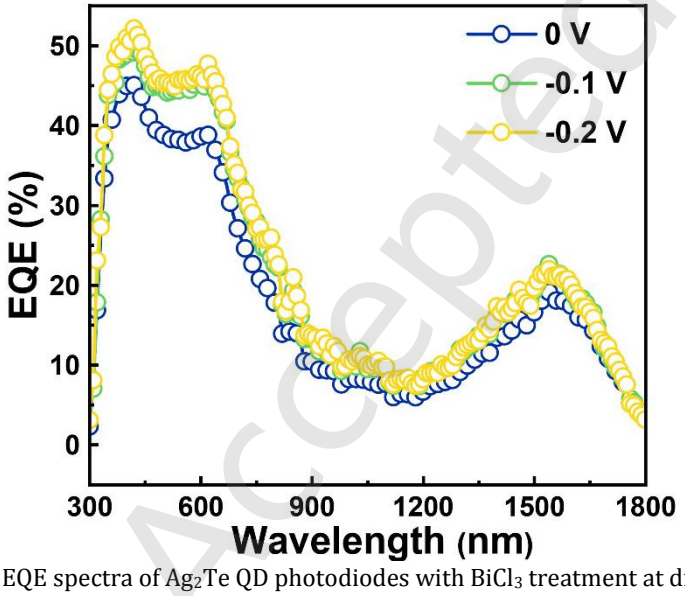

Figure S17. EQE spectra of Ag_2Te QD photodiodes with $BiCl_3$ treatment at different bias.

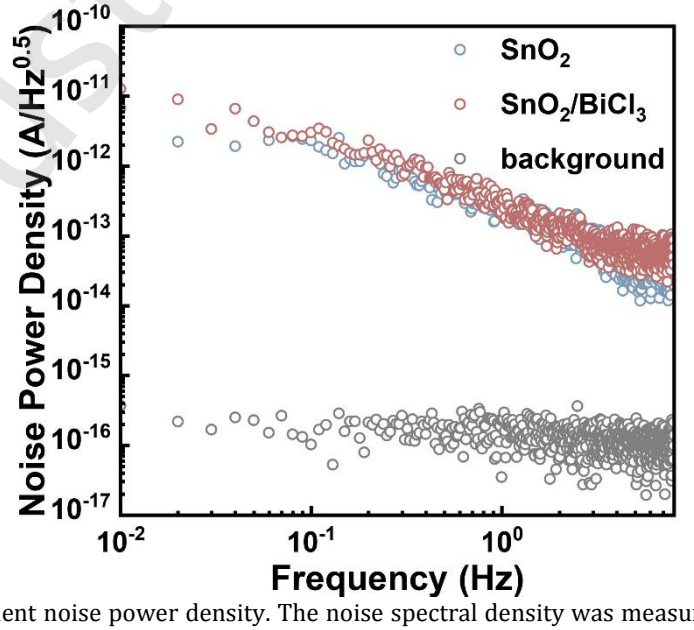

Figure S18. Frequency dependent noise power density. The noise spectral density was measured using a low frequency noise test system (LFN-2000) in RMS average mode with an extremely low noise background of 10^{-16} $A/Hz^{0.5}$.

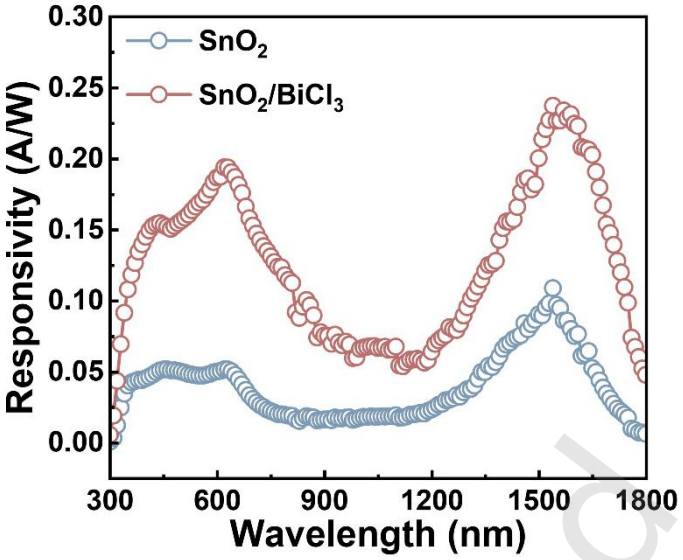

Figure S19. Responsivity of Ag_2Te QD photodiodes with and without $BiCl_3$ treatment.

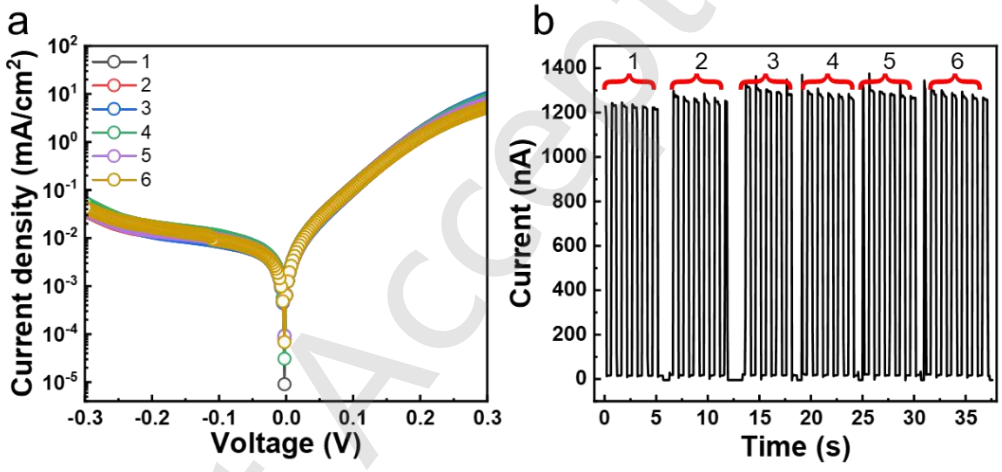

Figure S20. (a) Dark current density-voltage (J-V) curves of 6 points on the photodiodes with $BiCl_3$ treatments. (b) On-off characteristics under short-circuit conditions with a 1532 nm irradiation of 6 points on the photodiodes with $BiCl_3$ treatments

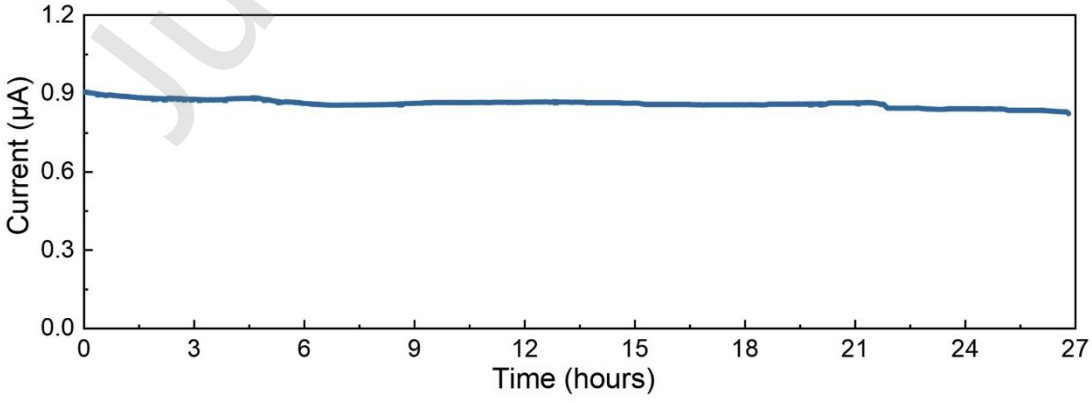

Figure S21. The photoresponse stability of the $BiCl_3$-treated photodiode measured with under 808 nm illumination with power densities of 0.05 mW cm^{-2}.

Table S1. EIS parameters of control and $BiCl_3$-modified devices.

Devices	R_s (Ω)	R_{rec} (Ω)
Control	60	1682
$BiCl_3$-modified	57	8563

Table S2. EIS parameters of control and $BiCl_3$-modified devices.

Sample	Adsorbed O	Vacancy O	Lattice O
SnO_2	18%	75%	7%
$SnO_2/BiCl_3$	31%	45%	24%

Table S3. Trap density and electron mobility of control and $BiCl_3$-modified devices according to Figure 2c.

Devices	Trap density (cm^{-3})	Electron mobility ($cm^2 V^{-1} s^{-1}$)
Control	4.31×10^{15}	0.76×10^{-3}
$BiCl_3$-modified	1.32×10^{15}	1.95×10^{-3}

Table S4. Performance statistics of the previously reported QDs SWIR photodetector.

QD Materials	Device area	Dark current	Peak EQE	Response time	D* (Jones)	Ref.
InAs	10 mm^2	10 $\mu A/cm^2$ @-1 V	15% @1450 nm, 1 V	1.06 μs	1.2×10^{10} @10Hz	[2]
InSb	NA	14 $\mu A/cm^2$ @-1 V	33% @1380 nm, 1 V	2.3 μs	1×10^{12} @2kHz	[3]
InSb	NA	45 $\mu A/cm^2$ @-1 V	28% @1450 nm, 1 V	2.5 μs	1.2×10^{10} @10 kHz	[4]
Ag_2Te	3.1 mm^2	2 $\mu A/cm^2$ @-0.3 V	20% @1400 nm, 0 V	1.3 μs	10^{10} @1Hz	[5]
Ag_2Te	1 mm^2	0.4 $\mu A/cm^2$ @-0.3 V	20% @1450 nm, 0 V	~600 ns	1.1×10^{11} @1Hz	[6]
Ag_2Te	NA	40 mA/cm^2 @-0.3 V	16% @1700 nm, 0.3 V	10.6 μs	9.0×10^{10} @10kHz	[7]
Ag_2Te	10 mm^2	110 $\mu A/cm^2$ @-1 V	0.21%@1550 nm @0 V	0.2 μs	6.1×10^{6} @10kHz	[8]
Ag_2Te	1 mm^2	60 $\mu A/cm^2$ @-0.3 V	2.5%@1550 nm @0 V	~97 μs	1.4×10^{8} @10Hz	[9]
Ag_2Te	6 mm^2	50 $\mu A/cm^2$ @-0.3 V	20% @1540 nm, 0 V	~10 μs	2.3×10^{11} @1Hz	*This work*

References

[1] Jiang, Y.; Cui, M.; Li, S.; Sun, C.; Huang, Y.; Wei, J.; Zhang, L.; Lv, M.; Qin, C.; Liu, Y.; Yuan, M. Reducing the impact of Auger recombination in quasi-2D perovskite light-emitting diodes. *Nat. Commun*. **2021**, *12*, 336.

[2] Sheikh, T.; Mir, W. J.; Alofi, A.; Skoroterski, M.; Zhou, R.; Nematulloev, S.; Hedhili, M. N.; Hassine, M. B.; Khan, M. S.; Yorov, K. E.; Hasanov, B. E.; Liao, H.; Yang, Y.; Shamim, A.; Abulikemu, M.; Mohammed, O. F.; Bakr, O. M. Surface-reconstructed InAs colloidal nanorod quantum dots for efficient deep-shortwave infrared emission and photodetection. *J. Am. Chem. Soc.* **2024**, *146*, 29094–29103.

[3] Imran, M.; Kim, D. B.; Xia, P.; Villanueva, F. Y.; Rehl, B.; Pina, J. M.; Liu, Y.; Zhang, Y.; Voznyy, O.; Kumacheva, E.; Hoogland, S.; Sargent, E. H. Control over metal-halide reactivity enables uniform growth of InSb colloidal quantum dots for enhanced SWIR light detection. *Adv. Mater.* **2025**, *37*, 2420273.

[4] Zhang, Y.; Imran, M.; Xia, P.; Chen, Y.; Gulsaran, A.; Liu, Y.; Nikbin, E.; Rehl, B.; Fan, L.; Dinic, F.; Kim, D. B.; Zeng, L.; Yavuz, M.; Hoogland, S.; Sargent, E. H. Nucleophilic Covalent Ligands Enable Simultaneous Surface Reconstruction and Passivation of Colloidal InSb Quantum Dots for Stable Short-Wave Infrared Photodetectors. *Angew. Chem. Int. Ed.* **2025**, *64*, e202505179.

[5] Wang, Y.; Peng, L.; Schreier, J.; Bi, Y.; Black, A.; Malla, A.; Goossens, S.; Konstantatos, G. Silver telluride colloidal quantum dot infrared photodetectors and image sensors. *Nat. Photonics* **2024**, *18*, 236–242.

[6] Wang, Y.; Wu, H.; Rodà, C.; Peng, L.; Taghipour, N.; Dosil, M.; Konstantatos, G. Shortwave infrared light detection and ranging using silver telluride quantum dots. *Adv. Mater.* **2025**, *37*, 2500977.

[7] Kim, G.; Choi, D.; Eom, S. Y.; Jung, E. D.; Lee, J. H.; Rehl, B.; Kim, S. Y.; Hoogland, S.; Sargent, E. H.; Jeong, K. S. Extended short-wavelength infrared ink by surface-tuned silver telluride colloidal quantum dots and their infrared photodetection. *ACS Mater. Lett.* **2024**, *6*, 4988–4996.

[8] Ahn, Y.; Eom, S. Y.; Kim, G.; Lee, J. H.; Kim, B.; Kim, D.; Si, M.; Yang, M.; Jung, Y.; Kim, B. S.; Chung, Y. J.; Jeong, K. S.; Baek, S. Silver telluride colloidal quantum dot solid for fast extended shortwave infrared photodetector. *Adv. Sci.* **2024**, *11*, 2407453.

[9] Yuan, D.; Cao, F.; Han, Z.; Liu, M.; Deng, X.; Zhang, L.; Liu, X.; Cao, S.; Liu, X.; Yang, Z.; Deng, Z.; Li, Y.; Voznyy, O.; Fan, Q.; Sun, B.; Huang, W. Zinc halide enables highly monodisperse Ag_2Te colloidal quantum dots for short-wave infrared photodetectors. *Nano Energy* **2025**, *140*, 111026.